Total cross section and resonance spectroscopy for $n + {}^{122}Sn$

R. F. Carlton
Department of Physics & Astronomy, Middle Tennessee State University, Murfreesboro, Tennessee 37132

J. A. Harvey and N. W. Hill
Oak Ridge National Laboratory, Oak Ridge, Tennessee 37831

(Received 6 April 1995)

The neutron total cross section of ^{122}Sn has been measured over the energy range 0.013 to 0.310 MeV. An R-matrix analysis has been performed to obtain resonance and average parameters which provide for a complete representation of the neutron entrance channels for the $s_{1/2}$, $p_{1/2}$, and $p_{3/2}$ contributions. The conventional s- and p-neutron strength functions have been determined to be 0.123 ± 0.023 and 2.0 ± 0.2, respectively (in units of 10^{-4}). Limits are placed on the average level spacings and strength functions for the individual partial wave components. The s-wave potential scattering radius has been determined to be 6.3 ± 0.1 fm. Average scattering functions, deduced from the average parameters, have been used to determine the real well depth of an optical model potential which reproduces these functions. We find, as have others, that the real well depth is parity dependent.

PACS number(s): 25.40.Dn, 24.10.Ht, 24.30.Gd, 27.60.+j

I. INTRODUCTION

The isotopes of tin have been the subject of numerous investigations because of the possibility of systematic studies of nuclear structure, the magic and near-magic number of nucleons, and the consequent simplification of model investigations. Kisslinger and Sorensen [1] have performed model calculations of the level structure and properties of tin isotopes in the bound region. The model includes long and short range (pairing) interactions for a realistic succession and separation of the low-lying single-particle levels which are available to the particles outside of closed shells. Many of the systematic features of the calculated quantities were in good agreement with experimental values. Baranger [2] summarized systematic trends in both experimental and shell model features for the tin isotopes.

Fuketa and Harvey [3] made the first systematic measurements of neutron transmission measurements of all of the tin isotopes many years ago at the Oak Ridge chopper up to a neutron energy of 10 keV. Though these measurements revealed few resonances above 2 keV, many interesting features were observed in this narrow energy interval. They found the s-wave strength functions to be lower than both that for other elements in this mass region, and predictions based on an optical model with high absorption at the nuclear surface. Harvey and Fuketa [4] confirmed strong isolated p-wave resonances and associated $M1$ radiation in several of the isotopes. Shakin [5] interpreted this as evidence for p-wave doorway structure in the tin isotopes. By summing calculated strengths of three-quasiparticle $1/2^+$ model states over an energy region centered at the neutron binding energy the low energy s-wave strength functions were well reproduced when the energy range over which the strength of a quasiparticle state is spread when the residual interaction between the particles was taken into account was approximately 3 MeV.

Nuclear levels in the unbound region are not well explored for tin. High resolution neutron total cross section measurements on zero-spin nuclei at energies above 10 keV, where one expects other than s-wave interaction, can be used to identify the positions and strengths of $1/2^+$, $1/2^-$, and $3/2^-$ levels in this region and provide information for the refinement of model calculations. Extension to higher energies will also permit the investigation of possible doorway structure in the s-wave interaction channel.

Another useful feature of the Sn isotopes is the provision offered for studying the isospin dependence of various nuclear properties. Numerous scattering and total cross section measurements at both low and high neutron energies have been carried out and optical model parameters deduced from fits to the data. None of these studies have resolved l- and J-specific contributions. Only in the process of fitting the total data set have s- and p-wave strength functions and scattering radii been deduced in some cases.

Most recently a study [6] of $^{116,120}Sn$ differential elastic and inelastic scattering cross sections and analyzing powers in the energy range 10–24 MeV has been analyzed together with total cross section measurements from 10 keV to 100 MeV to more definitively determine the parameters of a deformed optical model potential to be used in the framework of a coupled channels formalism for vibrational nuclei. This analysis also included known s- and p-wave strength function information. An l dependence was not considered in deducing the potential parameters but it was noted that the model overestimated the p-wave strength by approximately 40%.

The present study, while not encompassing a large energy range, is the most extensive high-resolution measurement which extends into the 100 keV region. Very detailed information in the form of individual partial wave contributions is made possible through the high-energy resolution of the Oak Ridge Electron Linear Accelerator (ORELA). This partial-wave specific information can be used to determine average

TABLE I. Isotopic enrichment of ^{122}Sn. Thickness = 0.073 atoms/barn.

Isotope	% present
112	<0.02
114	<0.02
115	0.02
116	1.01
117	0.58
118	1.91
119	0.77
120	3.75
122	90.8
124	1.16

nuclear properties for individual J^{π} interactions and to test for l dependence of the nuclear potential.

We discuss the experimental details of the measurement in Sec. II. In Sec. III we give the experimental results and in Sec. IV the details of the connection between the R-matrix parametrization and the experiment. We also discuss the bases of the resonance spin and parity assignments. Section V presents the resonance and nonresonance average properties deduced. Section VI presents the results of comparison of the deduced average scattering functions with predictions of a spherical optical model potential (OMP). Finally we discuss the OMP results in the context of other studies in Sec. VII and the paper concludes with Sec. VIII.

II. EXPERIMENTAL MEASUREMENTS

We have performed transmission measurements by the time-of-flight technique, using neutron pulses from the Oak Ridge Electron Linear Accelerator, at a flight path of 200 m for a target of ^{122}Sn. The 140 MeV electron beam burst width was 15 nsec and the accelerator was pulsed at 800 bursts per sec at a power level of approximately 20 kW. The resulting neutron burst has a continuous energy spectrum produced by the photoneutron process in tantalum with subsequent moderation in the 15-cm-diam., beryllium-clad, water-filled target housing. Collimation was used to select neutrons from the water-moderated region of the target. The neutron energy resolution function is expected to be a combination in quadrature of the fluctuations in flight-path length and apparent flight time and has been found to have an approximately Gaussian shape with a full width at half maximum dE given by

$$(dE/E)^2=(0.16+4E)\times 10^{-6},$$

with E expressed in MeV. Overlap neutrons were eliminated by a 1-g/cm^2 ^{10}B filter and gamma rays were reduced by a 0.73-cm-thick ^{238}U filter, placed 5 m from the neutron source.

The 29.914 g sample of ^{122}Sn was 1.59 cm in diameter, corresponding to a thickness of 13.70 barns/atom. Table I gives the sample enrichment and thickness. We performed additional measurements on a sample of natural tin in order to identify possible impurities in the sample due to the other isotopes of tin. The samples were positioned 9 m from the neutron target where the neutron beam was collimated to a diameter of 1.4 cm. The samples were cycled into and out of the neutron beam under computer control with a cycle time of approximately 10 min per sample. A 10-min run per cycle was also made with no sample in the beam. We used a neutron monitor to compensate for fluctuations in the neutron production rate during the 10 d interval and a total of 226 h of data collection. The five individual runs were each corrected for deadtime and then added to form the final data set.

Neutrons were detected by a NE110 proton recoil detector 7.6 cm in diameter and nominally 2-cm thick. The plastic scintillator was optically coupled to an RCA 8854 photomultiplier tube which was operated in a "selective gating" mode. In this mode, four neutron energy windows are established, the crossover energies between these windows being 230, 630, and 2020 keV. Logic for gating event deadtime in the time digitizer is then determined as follows: (a) a single-stop-per-start if an event was identified in time as a gamma flash and occurred in windows 1, 2, or 3 and (b) an event occurred in window 3 at any time. If the event occurred anywhere else, the system operated in a multi-stop-per-start

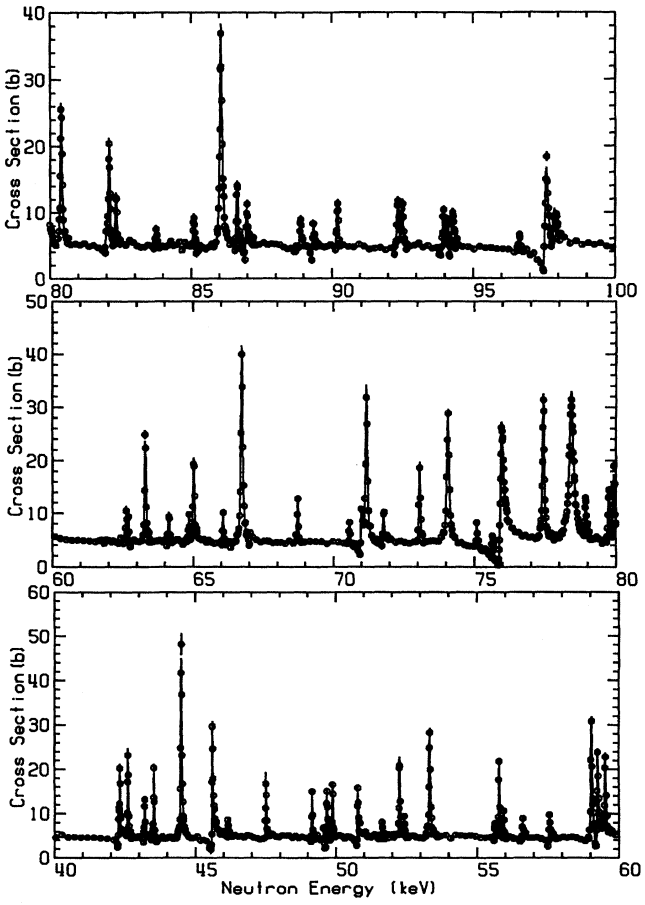

FIG. 1. Total neutron cross sections over selected energy regions. The symbols correspond to experimental measurements and the smooth curves correspond to R-matrix parametrization of the data. Symbols without error bars have errors within the size of the symbol.

TABLE II. R-matrix resonance parameters for $n+{}^{122}$Sn for the energy range 13–310 keV.

Energy (keV)	J^π	$g\Gamma_n$ (eV)	$g\gamma_n^2$ (eV)	Energy (keV)	J^π	$g\Gamma_n$ (eV)	$g\gamma_n^2$ (eV)	Energy (keV)	J^π	$g\Gamma_n$ (eV)	$g\gamma_n^2$ (eV)
13.231	$(3/2^-)$	5	472	35.256	$(1/2^-)$	2	38	53.332	$3/2^-$	37	436
13.818	$(3/2^-)$	5	429	35.393	$1/2^+$	1	1	55.628	$(1/2^-)$	3	35
15.061	$(3/2^-)$	3	209	35.440	$1/2^-$	27	567	55.783	$(3/2^-)$	23	261
15.079	$(3/2^-)$	4	310	35.568	$1/2^+$	8	13	55.934	$(3/2^-)$	8	85
15.866	$(3/2^-)$	4	248	36.863	$(1/2^-)$	5	106	56.591	$1/2^+$	5	6
17.150	$(3/2^-)$	3	175	37.387	$(3/2^-)$	9	180	57.534	$1/2^+$	6	8
18.104	$(1/2^-)$	4	195	38.193	$(1/2^-)$	1	25	59.038	$1/2^-$	41	426
18.962	$1/2^+$	9	21	38.584	$1/2^-$	50	945	59.122	$(3/2^-)$	9	88
19.418	$(1/2^-)$	3	152	42.265	$1/2^+$	4	6	59.238	$1/2^+$	26	34
20.634	$1/2^+$	4	10	42.318	$3/2^-$	12	191	59.524	$(3/2^-)$	28	288
22.136	$(3/2^-)$	4	161	42.603	$(1/2^-)$	13	211	62.626	$(1/2^-)$	8	73
22.907	$(1/2^-)$	11	424	43.197	$(3/2^-)$	7	115	62.705	$(3/2^-)$	6	56
24.125	$(1/2^-)$	6	231	43.520	$(3/2^-)$	12	191	63.299	$3/2^-$	39	369
24.510	$(3/2^-)$	6	202	44.497	$3/2^-$	50	764	64.140	$(3/2^-)$	9	85
26.278	$(1/2^-)$	4	116	45.594	$1/2^+$	23	35	64.851	$(3/2^-)$	9	80
27.102	$1/2^+$	36	69	46.151	$(3/2^-)$	3	44	65.021	$1/2^-$	29	262
27.118	$(1/2^-)$	4	116	47.471	$1/2^+$	2	4	66.073	$(3/2^-)$	8	75
28.281	$3/2^-$	17	497	47.510	$1/2^-$	8	118	66.735	$3/2^-$	88	772
28.423	$1/2^-$	12	335	49.154	$(3/2^-)$	10	135	68.730	$(3/2^-)$	16	132
28.889	$(1/2^-)$	3	76	49.567	$(3/2^-)$	4	50	70.576	$(3/2^-)$	8	69
31.591	$1/2^+$	13	23	49.666	$1/2^+$	10	14	70.987	$1/2^+$	13	16
31.869	$1/2^-$	11	281	49.885	$(3/2^-)$	12	157	71.182	$3/2^-$	70	564
32.337	$1/2^-$	26	620	50.765	$1/2^+$	11	16	71.765	$1/2^+$	9	10
33.288	$1/2^+$	2	4	51.629	$1/2^+$	2	3	73.065	$3/2^-$	33	258
34.453	$(3/2^-)$	7	145	52.265	$(3/2^-)$	23	281	74.072	$1/2^-$	75	568
34.994	$(1/2^-)$	8	179	52.424	$(1/2^-)$	4	46	75.093	$(3/2^-)$	10	75

mode with an 1104 nsec deadtime. Additional details concerning the data acquisition have been reported in detail elsewhere [7]. These separate pulse height spectra facilitated the determination of the backgrounds and the optimization of the signal to background ratio.

We monitored four sources of background during the experiment: (1) 2.2 MeV gamma rays in the beam produced by neutron capture in the water moderator, (2) a constant beam-independent background, (3) a 478-keV gamma ray from the ^{10}B$(n,\alpha\gamma)$ reaction resulting from neutrons moderated by the NE110 plastic scintillator and then absorbed by the boron in the Pyrex face of the photomultiplier, and (4) delayed pulses within the photo tube and scintillator. A discussion of these and other experimental details may be found elsewhere [8]. The transmission was computed from the background-corrected sample-in and sample-out ratio, normalized to the corresponding neutron monitor counts.

III. RESULTS

As a representative sample of the results for ^{122}Sn, Fig. 1 shows the energy range 40–100 keV. The uncertainties in the data are shown as vertical lines or are less than the size of the symbols. The solid line represents the R-matrix parametrization of the total cross section discussed in the next section. Strong interference patterns are seen at 45, 76, and 97 keV, characteristic of s-wave interaction. The non-s-wave resonance at 86 keV must be due to $p_{3/2}$ interaction, because the peak cross section at this energy is approximately 34 b for interactions having a spin statistical factor $g_J=1$. The peak-to-valley cross section is seen in the figure to be 38 b. Since the spin statistical factor is *unity* for $p_{1/2}$ resonances, the peak must be due to $p_{3/2}$ or higher. In this way the J^π values are established for the large resonances. Since the target was not a pure sample of ^{122}Sn, the contributions of impurity isotopes may not be insignificant. At these energies, the contribution to the total background cross section is primarily due to the s-wave interaction. We have thus included off-resonance s-wave contributions due to $^{116-124}$Sn, the largest impurity components. At 50–100 keV neutron energies, this contribution to the background cross section amounts to approximately 0.5 b. Contributions from other partial waves of the impurity components are small at these energies, in comparison to the s waves. The resonance contributions to the cross sections from the impurity isotopes will be negligible for all but those of very large width. We have performed measurements on a sample of natural tin to determine the energies of such resonances to account for some of the broad structure seen in the ^{122}Sn data.

The early transmission measurements [3] observed a total of nearly 100 resonances in *all* the stable isotopes of tin up to a neutron energy of 10 keV. In the present case we have extended the energy range to 310 keV, and the number of resonances to 347 for just one isotope. From the multilevel resonance analysis we have obtained spin-separated resonance and nonresonant parameters. We have made parity *and*

TABLE II. (*Continued.*)

Energy (keV)	J^π	$g\Gamma_n$ (eV)	$g\gamma_n^2$ (eV)	Energy (keV)	J^π	$g\Gamma_n$ (eV)	$g\gamma_n^2$ (eV)	Energy (keV)	J^π	$g\Gamma_n$ (eV)	$g\gamma_n^2$ (eV)
75.651	$(3/2^-)$	8	62	97.545	$1/2^+$	61	62	121.911	$3/2^-$	71	283
75.942	$1/2^+$	87	101	97.816	$1/2^+$	14	14	122.575	$3/2^-$	119	467
77.436	$3/2^-$	72	514	101.854	$1/2^-$	183	914	123.561	$(3/2^-)$	57	223
78.426	$1/2^-$	151	1064	102.719	$3/2^-$	33	163	124.058	$1/2^+$	25	23
78.925	$(3/2^-)$	18	127	104.200	$(1/2^-)$	22	107	125.687	$(1/2^-)$	52	199
79.739	$(1/2^-)$	19	134	104.475	$1/2^+$	10	10	126.111	$(1/2^-)$	11	41
79.747	$1/2^+$	5	6	105.156	$(1/2^-)$	12	56	126.730	$(1/2^-)$	24	89
79.919	$1/2^-$	27	188	106.892	$1/2^+$	23	22	127.488	$3/2^-$	210	784
80.390	$3/2^-$	59	400	107.026	$(1/2^-)$	25	119	127.530	$1/2^+$	7	7
81.973	$1/2^+$	5	6	108.262	$(3/2^-)$	56	259	129.509	$(3/2^-)$	59	215
82.088	$3/2^-$	39	261	108.471	$1/2^+$	4	4	130.596	$(3/2^-)$	53	192
82.327	$3/2^-$	19	128	108.624	$(1/2^-)$	77	354	132.445	$1/2^-$	121	431
83.743	$(3/2^-)$	3	19	108.982	$(1/2^-)$	43	196	133.280	$(3/2^-)$	28	99
85.091	$(3/2^-)$	13	81	110.786	$(1/2^-)$	41	182	134.853	$(1/2^-)$	60	208
86.054	$3/2^-$	122	757	113.549	$(3/2^-)$	97	422	135.480	$(1/2^-)$	8	26
86.621	$(3/2^-)$	27	168	114.058	$(3/2^-)$	39	170	136.158	$(1/2^-)$	16	56
86.950	$1/2^+$	14	15	114.444	$3/2^-$	60	258	137.624	$(1/2^-)$	37	125
88.892	$(3/2^-)$	14	81	114.961	$3/2^-$	144	612	137.948	$3/2^-$	254	860
89.319	$1/2^+$	8	8	115.498	$1/2^+$	13	13	140.181	$(1/2^-)$	21	71
90.198	$(3/2^-)$	20	119	116.707	$(3/2^-)$	19	79	141.351	$(1/2^-)$	20	65
92.348	$(3/2^-)$	30	169	117.372	$(3/2^-)$	74	306	141.776	$1/2^+$	3	3
92.488	$(3/2^-)$	25	142	118.507	$(3/2^-)$	19	77	141.882	$(1/2^-)$	53	174
93.964	$(1/2^-)$	19	107	118.509	$1/2^+$	2	2	143.809	$(1/2^-)$	37	120
94.098	$(1/2^-)$	14	79	118.778	$(3/2^-)$	45	185	144.443	$(3/2^-)$	17	56
94.243	$1/2^+$	16	16	120.389	$(3/2^-)$	44	177	145.387	$1/2^+$	27	23
96.629	$(3/2^-)$	8	43	121.567	$(3/2^-)$	18	70	145.412	$(1/2^-)$	103	325

spin assignments for many of the observed resonances, where earlier results were only able to distinguish s-wave resonances. Besides the normally reported strength functions and level spacings, our R-matrix analysis yields average properties describing the resonances outside the region as deduced from their influence in the region through observed resonance asymmetries. We deduced these parameters for the $s_{1/2}$, $p_{1/2}$, and $p_{3/2}$ partial wave components. Since the external R function is related to the real part of the optical model potential, we are able to deduce some of the parameters of this potential, extending previous investigations [9] of the l dependence of the real well depth of the optical model potential.

Table II gives the resonance parameters for $n+{}^{122}$Sn. We have analyzed 347 resonances up to an energy of 310 keV, where spin assignments became more uncertain and multiplet structure more common. There are regions where the data would support additional small resonances, but we have not been able to determine if these are due to impurity resonances or weak multiplet structure. Their inclusion would only significantly impact the level spacing and not the strength. We have thus ignored them. This isotope is in a region of very low s-wave strength function and our results confirm that fact with smaller uncertainty than past measurements.

IV. *R*-MATRIX ANALYSIS

For the case where radiative capture is negligible and only one neutron channel is open, we can write the total cross section in terms of real phase shifts, δ_{lJ}, as

$$\sigma_T(E)=\sum_{lJ}\frac{4\pi}{k^2}g_J\sin^2\delta_{lJ}(E), \tag{1}$$

where g_J is the statistical spin factor and k is the neutron wave number. To fit the data we parametrize the phase shifts using the R-matrix formalism,

$$\delta_{lJ}(E)=\phi_l(E)+\tan^{-1}[P_l(E)R_{lJ}(E)], \tag{2}$$

where we have set the boundary condition B_{lJ} equal to the shift factor at all energies and where P_l and ϕ_l are, respectively, the lth-wave penetrability and hard-sphere phase shift evaluated at the chosen boundary radius, taken to be $1.45\times A^{1/3}$ fm.

The R function is a sum over the observed resonances plus a smoothly increasing function of energy which describes the aggregate effect of levels external to the region of measurement,

$$R_{lJ}(E)=\sum_{\lambda=1}^{N}\frac{\gamma^2_{\lambda lJ}}{E_{\lambda lJ}-E}+R^{\rm ext}_{lJ}(E), \tag{3}$$

where γ^2_{lJ} and E_{lJ} are free parameters representing the reduced width and energy of the λth resonance, with the γ^2_{lJ} related to the neutron widths Γ_n by the relation

TABLE II. (*Continued.*)

Energy (keV)	J^π	$g\Gamma_n$ (eV)	$g\gamma_n^2$ (eV)	Energy (keV)	J^π	$g\Gamma_n$ (eV)	$g\gamma_n^2$ (eV)	Energy (keV)	J^π	$g\Gamma_n$ (eV)	$g\gamma_n^2$ (eV)
146.166	$(1/2^-)$	48	150	164.193	$1/2^+$	13	10	180.337	$1/2^-$	76	185
147.506	$(1/2^-)$	75	234	164.310	$(3/2^-)$	90	247	180.713	$3/2^-$	98	238
149.138	$(3/2^-)$	46	141	165.150	$1/2^+$	15	12	181.122	$1/2^+$	4	3
150.323	$1/2^+$	5	4	165.178	$(3/2^-)$	28	77	181.233	$3/2^-$	188	457
150.458	$(1/2^-)$	60	183	165.753	$(1/2^-)$	21	58	182.240	$3/2^-$	104	251
151.228	$(1/2^-)$	57	174	166.652	$(3/2^-)$	110	294	183.420	$1/2^-$	249	596
151.566	$1/2^+$	4	3	166.726	$1/2^+$	31	24	183.830	$(1/2^-)$	17	40
152.834	$(3/2^-)$	43	128	167.025	$(3/2^-)$	107	286	185.302	$(1/2^-)$	34	80
153.100	$1/2^+$	8	6	167.426	$(3/2^-)$	70	187	185.806	$(3/2^-)$	9	21
154.060	$(3/2^-)$	29	87	168.100	$1/2^+$	12	9	186.343	$3/2^-$	41	96
154.285	$(3/2^-)$	10	31	169.405	$3/2^-$	60	158	186.748	$1/2^-$	160	375
155.139	$(3/2^-)$	49	144	170.035	$1/2^+$	6	5	187.329	$(3/2^-)$	41	96
156.040	$1/2^+$	46	37	170.110	$3/2^-$	40	104	187.921	$(1/2^-)$	8	20
156.077	$(3/2^-)$	50	145	170.281	$(1/2^-)$	9	24	188.177	$1/2^+$	23	17
156.774	$(1/2^-)$	28	80	171.739	$(3/2^-)$	17	44	190.112	$1/2^-$	53	121
156.966	$(1/2^-)$	59	171	173.224	$1/2^+$	16	12	191.300	$3/2^-$	220	500
158.777	$(1/2^-)$	55	156	173.366	$(1/2^-)$	16	40	191.886	$1/2^+$	12	9
160.778	$(3/2^-)$	34	96	174.472	$(1/2^-)$	40	102	192.505	$(3/2^-)$	9	20
161.148	$(3/2^-)$	39	109	174.687	$(3/2^-)$	5	13	193.207	$(1/2^-)$	17	37
161.176	$1/2^+$	9	7	176.164	$(3/2^-)$	58	145	193.976	$(1/2^-)$	17	37
161.416	$(3/2^-)$	24	67	176.435	$1/2^+$	53	40	195.836	$(3/2^-)$	76	169
161.818	$1/2^+$	7	6	176.707	$(1/2^-)$	26	64	196.099	$(1/2^-)$	21	47
162.931	$(3/2^-)$	85	235	178.471	$(1/2^-)$	20	49	197.349	$(3/2^-)$	35	77
163.222	$(3/2^-)$	5	15	179.076	$(1/2^-)$	116	286	198.087	$(1/2^-)$	9	19
163.434	$1/2^+$	20	16	179.704	$1/2^+$	23	18	198.575	$3/2^-$	455	992
163.697	$(1/2^-)$	7	18	179.875	$(1/2^-)$	15	36	199.449	$(1/2^-)$	20	43

$$\gamma_{lJ}^2=\frac{\Gamma_{nlJ}}{2P_l}. \tag{4}$$

The external R function, in combination with ϕ_l, influences both the off-resonance cross section and the interference pattern of the resonances. We write this part of the R function as

$$R_{lJ}^{\text{ext}}(E)=\tilde{R}-\tilde{s}\,\ln\left[\frac{E_{\text{up}}-E}{E-E_{lo}}\right], \tag{5}$$

with the smooth function, $\tilde{R}$ parametrized as

$$\tilde{R}_{lJ}(E)=\alpha_{lJ}+\beta_{lJ}E \tag{6}$$

and α_{lJ} and β_{lJ} being free parameters. The log term accounts for resonances just outside the experimental region, $[E_{lo},E_{\text{up}}]$, and is equivalent to a continuous external distribution with a strength taken equal to the strength function, $\langle\gamma_{lJ}^2\rangle/D_{lJ}$, observed within $[E_{lo},E_{\text{up}}]$, where D_{lJ} is the average level spacing. This parametrization provides a simple procedure for averaging of the scattering function for comparison to the optical model. At low energy the s-wave smooth R function is related to the potential scattering length R_0' by

$$R_0'=a_c[1-\tilde{R}_0(E=0)], \tag{7}$$

where $\tilde{R}_0$ is evaluated for $E=0$. The $\tilde{R}_0$ obtained from fitting is dependent on the choice of channel radius a_c, but the value for R_0' is independent of that parameter. The final R-matrix parameters which best described the observed transmissions were determined by solving Bayes's equations using the R-matrix code SAMMY [10]. The fitting procedure included resolution broadening of the transmissions and Doppler broadening of the calculated cross sections, with an effective temperature of 306 K.

The s-wave resonances are easily distinguished by their characteristic asymmetry. We have assumed all other resonances to be due to p-wave interaction because of the small probability of d-wave interaction in this energy range. Three bases determined the p-wave spin assignments: (1) resonances with widths larger than the resolution width have peak-to-valley cross sections proportional to the g_J value; (2) resonances with widths comparable to the resolution width manifest some resonance-potential scattering interference asymmetry which decreases with increasing l value; (3) resonances with smaller width manifest resonance-resonance interference only if near a strong resonance of the same J^π. We used an iterative procedure to determine most of the J^π assignments, requiring the final assignment to provide a good description of the asymmetry patterns which arise from both resonance-resonance and resonance-potential scattering interference. The latter asymmetry serves to also determine the R^{ext} parameters for each partial wave for which there are one

TABLE II. (*Continued.*)

Energy (keV)	J^π	$g\Gamma_n$ (eV)	$g\gamma_n^2$ (eV)	Energy (keV)	J^π	$g\Gamma_n$ (eV)	$g\gamma_n^2$ (eV)	Energy (keV)	J^π	$g\Gamma_n$ (eV)	$g\gamma_n^2$ (eV)
200.364	$3/2^-$	185	399	220.787	$3/2^-$	242	466	243.788	$(1/2^-)$	37	64
201.623	$3/2^-$	151	324	221.422	$3/2^-$	91	175	244.207	$(3/2^-)$	62	106
201.864	$(1/2^-)$	40	85	221.498	$1/2^+$	26	17	245.304	$(1/2^-)$	125	214
202.463	$1/2^+$	20	14	222.382	$(1/2^-)$	25	47	245.756	$(3/2^-)$	86	146
203.219	$(1/2^-)$	70	149	223.224	$(3/2^-)$	81	154	246.079	$(1/2^-)$	160	272
205.197	$(1/2^-)$	71	148	224.413	$(1/2^-)$	47	88	249.857	$1/2^-$	702	1175
205.615	$(3/2^-)$	61	128	226.508	$(1/2^-)$	21	40	250.594	$3/2^-$	124	207
205.989	$(3/2^-)$	15	32	226.976	$(1/2^-)$	48	90	252.499	$3/2^-$	186	308
207.761	$1/2^+$	37	26	229.202	$1/2^-$	110	203	252.816	$(3/2^-)$	70	115
208.022	$1/2^-$	125	258	230.978	$1/2^-$	75	137	253.315	$(3/2^-)$	82	136
208.976	$(3/2^-)$	59	122	231.461	$(1/2^-)$	45	82	254.118	$(1/2^-)$	124	204
209.468	$(1/2^-)$	24	49	231.842	$(3/2^-)$	60	110	255.212	$(3/2^-)$	82	134
210.638	$3/2^-$	36	73	232.460	$(3/2^-)$	12	22	255.717	$(3/2^-)$	91	149
211.789	$1/2^-$	287	580	232.861	$(1/2^-)$	38	69	256.158	$3/2^-$	177	289
212.273	$(3/2^-)$	14	28	233.454	$(3/2^-)$	41	74	257.426	$(3/2^-)$	113	183
213.129	$(3/2^-)$	57	115	233.700	$1/2^+$	15	10	257.919	$(3/2^-)$	43	70
213.489	$(1/2^-)$	26	52	234.447	$(1/2^-)$	65	117	260.065	$(3/2^-)$	50	80
213.929	$(1/2^-)$	23	47	235.783	$3/2^-$	200	358	260.638	$3/2^-$	221	354
214.203	$3/2^-$	172	342	237.539	$(1/2^-)$	42	74	261.642	$(3/2^-)$	25	39
215.588	$3/2^-$	207	411	239.753	$(3/2^-)$	77	136	262.787	$3/2^-$	260	412
216.415	$(1/2^-)$	17	33	240.218	$(1/2^-)$	22	39	263.942	$(1/2^-)$	167	263
217.646	$1/2^+$	28	19	240.821	$(1/2^-)$	28	49	264.240	$(3/2^-)$	78	122
217.947	$3/2^-$	99	193	241.106	$1/2^+$	9	6	265.150	$1/2^+$	16	10
218.795	$3/2^-$	133	259	241.334	$1/2^-$	268	466	265.409	$(3/2^-)$	187	293
218.882	$1/2^+$	33	22	241.991	$1/2^+$	14	9	265.700	$(1/2^-)$	40	63
219.415	$(3/2^-)$	17	33	242.960	$(1/2^-)$	31	53	266.592	$(3/2^-)$	85	133

or more resonances manifesting sufficient asymmetry (in this case $s_{1/2}$-$p_{3/2}$). This is possible even in the case where only one large resonance exists in the region of analysis. Resonances whose spin assignments were uncertain are indicated in Table II with parentheses.

V. AVERAGE PROPERTIES

The average properties of interest in the analysis of neutron total cross section data are the strength functions, the level spacings, and the external R functions. These are related to interest in the statistical and optical models. We will treat each of these properties in turn.

A. Strength functions

The R-matrix strength functions $\tilde{s}$ are represented by the slopes of the plot of the cumulative reduced neutron width [see Eq. (4)] versus energy distribution, presented in Fig. 2 for the s- and p-wave resonances. In the case where the J-value samples are not pure, one considers the strength for a given l value. In the case of p waves, for example, the plot has the cumulative reduced neutron width replaced by the expression

$$g_J\gamma_\lambda^2/(2l+1), \tag{8}$$

where γ_λ^2 is the reduced neutron width of the λth resonance, and l is the orbital angular momentum quantum number. The slope of this curve gives the p-wave strength. The resulting values for $\tilde{s}$ differ by a factor of 15.

From the plots we can see that the strength functions are constant over the energy region, since a single line passed through the histograms would sufficiently describe the trend over a limited energy range. From the relation

$$\tilde{s}_l=\frac{\Sigma_{\lambda J}\, g_J\gamma_\lambda^2/(2l+1)}{\Delta E_l}, \tag{9}$$

the total p-wave strength is calculated to be $(7.8\pm 1.0)\times 10^{-2}$. This value is in excellent agreement with trends in this mass region. The value for the s-wave strength function, $(0.39\pm 0.07)\times 10^{-2}$, is an order of magnitude lower than that for the p waves but consistent with results for other isotopes of tin and with theoretical investigations of nuclear structure in this mass region. The corresponding values for the conventional strength function S_l are $(0.12\pm 0.02)\times 10^{-4}$ and $(2.0\pm 0.2)\times 10^{-4}$ for s and p waves, respectively.

In Fig. 3 we present the cumulative reduced neutron widths versus neutron energy for the individual p-wave components. There is an element of uncertainty in the apportionment of small resonances among the two spin states. The apportionment for these histograms was made on the basis of calculated χ^2 values, when fitting with each possibility, and the character of the resulting fits. It is seen that the strength for the $p_{1/2}$ component exceeds that of the $p_{3/2}$ by 30% de-

TABLE II. (*Continued.*)

Energy (keV)	J^π	$g\Gamma_n$ (eV)	$g\gamma_n^2$ (eV)	Energy (keV)	J^π	$g\Gamma_n$ (eV)	$g\gamma_n^2$ (eV)
268.144	$(3/2^-)$	107	166	296.106	$(1/2^-)$	37	51
268.365	$(1/2^-)$	48	74	298.264	$(1/2^-)$	146	202
271.975	$1/2^-$	225	342	298.620	$(3/2^-)$	118	163
272.873	$1/2^-$	77	116	298.977	$(1/2^-)$	97	133
274.544	$(1/2^-)$	33	50	301.763	$(3/2^-)$	192	262
275.307	$1/2^+$	37	22	305.601	$(1/2^-)$	350	470
276.031	$(1/2^-)$	153	230	308.781	$(1/2^-)$	81	107
276.839	$(3/2^-)$	87	129	309.073	$(1/2^-)$	206	273
277.591	$(3/2^-)$	70	104				
278.933	$(1/2^-)$	21	32				
280.195	$(1/2^-)$	105	155				
281.026	$(1/2^-)$	172	253				
281.967	$(1/2^-)$	76	112				
282.139	$1/2^+$	27	16				
284.670	$3/2^-$	190	276				
286.174	$(1/2^-)$	58	84				
286.590	$3/2^-$	340	489				
287.061	$(3/2^-)$	81	116				
287.800	$1/2^+$	35	21				
287.996	$(3/2^-)$	88	126				
289.026	$(3/2^-)$	61	88				
289.620	$(3/2^-)$	140	200				
290.338	$(3/2^-)$	82	116				
292.261	$(3/2^-)$	51	72				
293.641	$(3/2^-)$	115	161				
295.730	$(3/2^-)$	53	73				

spite the fact that the level density for the latter is greater. Such enhancement persists when including only resonances of definite spin and has been reported in similar studies on ^{86}Kr [11].

We have established lower limits for the individual $p_{1/2}$ and $p_{3/2}$ strength functions and level spacings by including only resonances whose peak height, resonance asymmetry, or close proximity to a large resonance made the J^π assignment definite. The upper limit, for each partial wave, comes from including all resonances of indefinite J^π in each of the spin groups, separately. Each of the p-wave spin groups constructed in this manner have 70–80 % of the resonances indefinite with approximately 50% of the resulting strength attributable to these uncertain resonances. Average resonance parameters, their statistical uncertainties, and their upper and lower limits are presented in Table III, in conventional units. The R-matrix strength functions $\tilde{s}$ will be discussed below in connection with the external R functions. The significance of this work is the reduced uncertainty on s- and p-wave strength functions and the lower and upper limits placed on the component p-wave strength functions and level spacings.

B. Level spacings

From the plot of the cumulative number of s-wave resonances in Fig. 4, we see that a total of 66 resonances were observed up to an energy of 310 keV. It would appear that up to approximately 240 keV, few resonances were missed. Above that energy the increased probability of p-wave interaction, coupled with the extremely low s-wave strength, results in missed s-wave resonances. We have not attempted a correction for the missed resonances, since their contributions to the strength is small. If the strength is calculated only up to the energy at which resonances begin to be missed, the result is within the statistical errors quoted in the table above.

The distribution of levels between the two p-wave spin states is inconsistent with the expected $2J+1$ dependence. This may be, in part, a consequence of the criterion used to apportion resonances between the two states where, for some small resonances, the differences in χ^2 values for different assumed J values were small and subject to random factors such as initial parameter estimates. A study of the Δ_3 statistic [12] applied to these levels could be useful as another criterion in reducing the number of uncertain spin states. The number of resonances is sufficiently large to merit an investigation of this statistic and model level densities, but we defer this to a future paper when level densities for other isotopes of tin are available. Histograms similar to those in Fig. 4 for only levels of definite J^π are consistent with the expected dependence, corroborating the suggestion of improper partitioning.

C. External R functions (R^{ext})

The R^{ext} are important parameters which represent the contributions, in the analyzed region, due to resonances out-

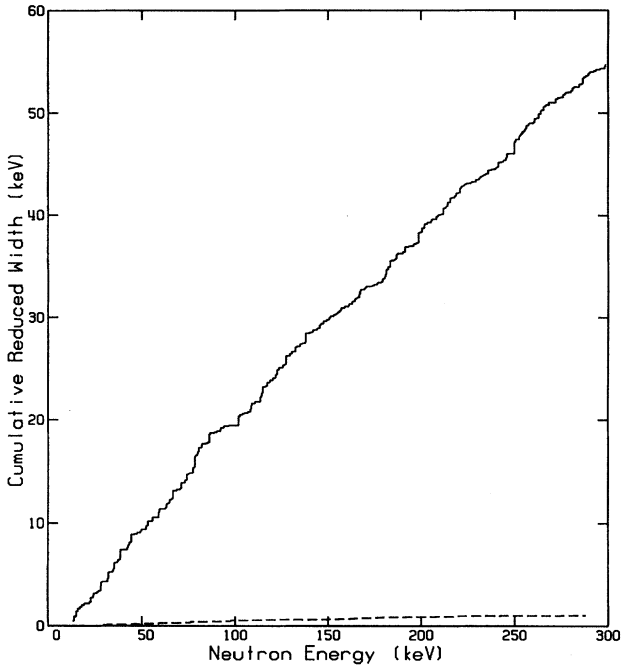

FIG. 2. s- and p-wave strength. The cumulative values for the p waves (solid histogram) represent that of Eq. (8). The slopes of the histograms give the strengths. The sum for s waves is only ≈ 1 keV.

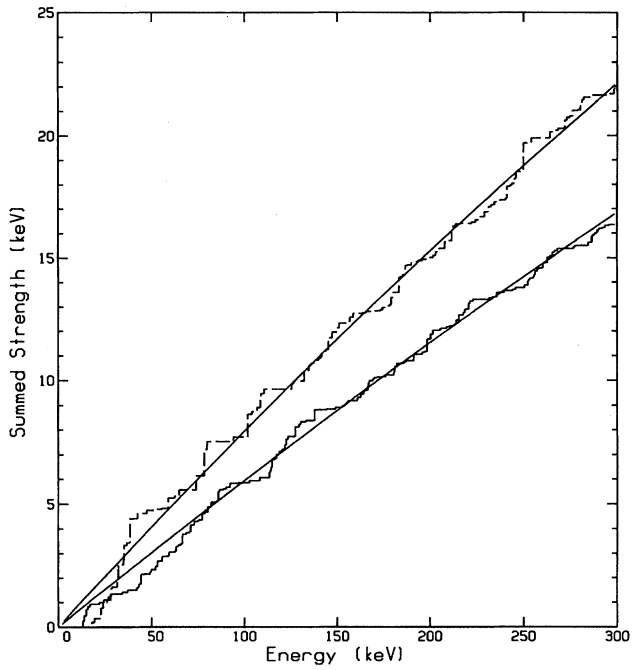

FIG. 3. Strength functions for p-wave components. The dashed histogram is for the $p_{1/2}$ partial wave. The slopes of these histograms give the corresponding strength functions. The solid lines represent optical model fits, discussed in Sec. VI.

side the region. These functions are related to the real part of the optical potential, and their general energy trends provide a constraint on the optical model parameters. In this nuclide distinction can be made between $p_{1/2}$ and $p_{3/2}$ *resonances* for only 25% of the non-s-wave resonances, with consequent uncertainty in the strengths deduced therefrom. The R^{ext}, however, can be deduced wherever a broad resonance of determined J^{π} occurs, and the number of such occurrences does not influence the uncertainty in the R^{ext} as much as in the case of the average resonance properties. The R^{ext} parameters and uncertainties for both these partial waves have been determined at the energies of resonances of known spin and parity. Their energy dependences are determined additionally by their influence on the background cross section throughout the energy range. At low energies the contribution to the off-resonance cross section is almost entirely due to s-wave potential scattering. As a consequence, the s-wave R^{ext} parameters are well determined through their influence upon the potential scattering radius, R_0' [see Eq. (7)]. A 10% change in the s-wave R^{ext}, for example, produces a visually distinguishable change in the total cross section in the 14–15 keV energy region. The maximum uncertainty for this parameter for s waves, for the entire energy region is 25%. Since concentrations of the isotopic impurities of the sample are lower by one to two orders of magnitude, compared to ^{122}Sn, their s-wave contributions to the off-resonance cross section will be correspondingly lower. Their contribution, through the R^{ext}, has nonetheless been included by setting impurity s-wave R^{ext} parameters equal to those found for ^{122}Sn.

Changes in the p-wave R^{ext} parameters of a factor of two have no noticeable effect on the observed off-resonance cross section or resonance asymmetries in the low energy region. At higher energies the p-wave influences become very discernable with regard to both the off-resonance cross section and the interference asymmetry of large p-wave resonances. Since the R_{lJ}^{ext} are related to the real part of the optical model potential, their values and uncertainties will influence the required well depth. We established the uncertainties by manual variation of the parameter α until a visual comparison showed noticeable disagreement with those asymmetries and nonresonant cross sections obtained from least squares parameters, in a region where the largest

TABLE III. Average resonance parameters for ^{122}Sn + n.

J^{π}	$S_J^l(\times 10^{+4})$ [a]	D (keV)
s	0.12(2) [b]	4.1(3)
p	2.0(2)	1.06(3)
$p_{1/2}$	$2.4(3)^{4.1}_{1.4}$	$2.4(1)^{10.2}_{1.3}$
$p_{3/2}$	$1.8(2)^{2.4}_{1.0}$	$1.8(1)^{5.9}_{1.1}$

[a]The conventional strength is given by $S_{lJ}=\langle\Gamma_{nJ}^l\rangle/D_{lJ}$, with $\Gamma_{nJ}^l=(1\ \text{eV}/E_{\lambda lJ})^{1/2}(\Gamma_{\lambda J}/v_l)$. D_{lJ} is the level spacing and v_l is the neutron penetrability. For the S_l, this expression is modified as in Eq. (9).

[b]In our notation, 0.12(2) is equivalent to 0.12 ± 0.02 and $2.4(3)^{4.1}_{1.4}$ indicates that upper and lower limits are 4.1 and 1.4, respectively, as discussed in the text. The numbers in parentheses represent statistical uncertainties.

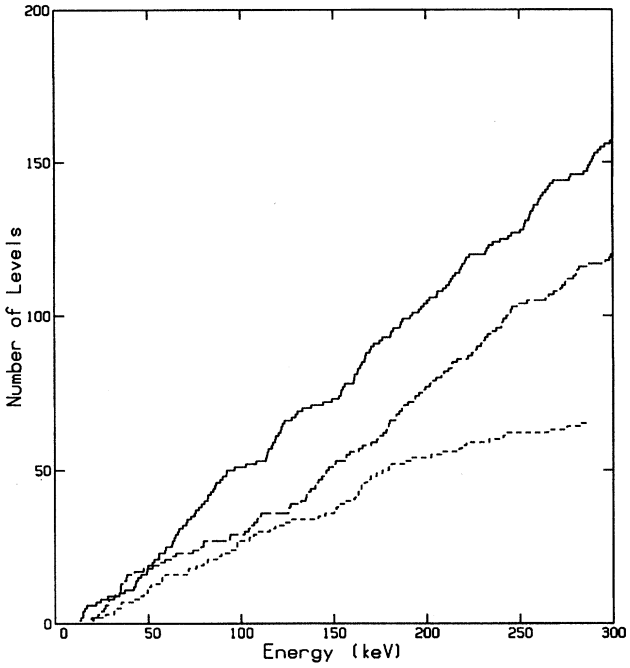

FIG. 4. Cumulative number of levels versus neutron energy for the $s_{1/2}$ (- - -), $p_{1/2}$ (– –), and $p_{3/2}$ (—) resonances. The slope of the histograms gives the level density for that partial wave.

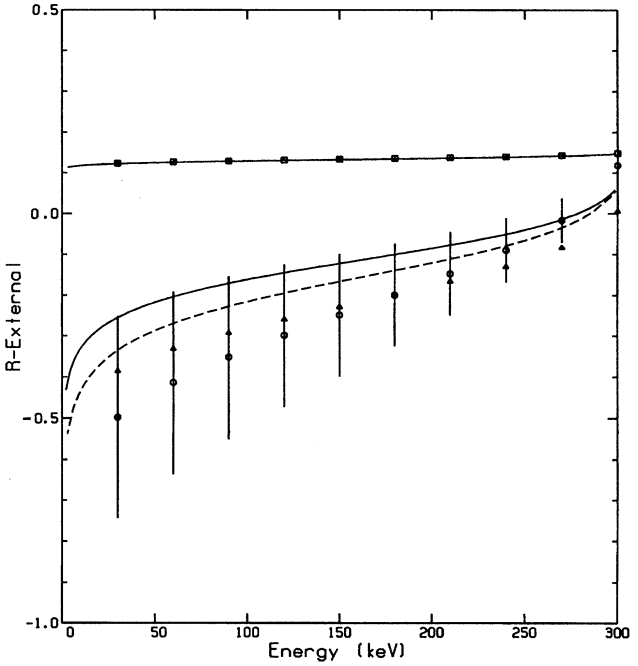

FIG. 5. The external R functions for the $s_{1/2}$ (□), $p_{1/2}$ (⊙), and $p_{3/2}$ (△) partial waves. The error bars for the $p_{3/2}$ are comparable to those shown for the $p_{1/2}$. Smooth curves represent optical model predictions (dashed curve for $p_{1/2}$).

resonance(s) of a given J^π occurred. Thus, while at 50 keV the p-wave parameters can be changed by a factor of 2 without noticeable change in the resonance asymmetry, at 80 keV the visually ascertained uncertainty is 50% and at 275 keV the uncertainty is approximately 10%. This variation has been parametrized and is reflected in error bars shown in Fig. 5. For clarity p-wave error bars are shown for only the $p_{1/2}$, those for the $p_{3/2}$ being the same. Error bars for the s waves are smaller than the symbol size. The $R^{\rm ext}$ parameters for the contributing partial waves are given in Table IV where the uncertainties in α and β are reflected through the value of the smooth R function $\tilde{R}_{lJ}$ at the midpoint of the energy region. The upper and lower limits for the R-matrix strength $\tilde{s}_{lJ}$ have been determined as discussed in Sec. V A.

VI. AVERAGE PARAMETERS AND THE OMP

Low energy neutron elastic scattering in the ^{122}Sn+n system serves as a probe of the optical model potential for each partial wave and is accomplished *via* the $R^{\rm ext}_{lJ}$ and $\tilde{s}_{lJ}$. The $R^{\rm ext}$ provide the dominant contribution to the real part V_r of the optical potential and the strength function is related to the surface imaginary depth W_D.

Energy-averaged scattering functions can be related to the average resonance parameters through the expression

$$\langle S_{lJ}(E)\rangle = e^{2i\phi_l(E)}\frac{[1+iP_l(E)\mathscr{R}_{lJ}(E)]}{[1-iP_l(E)\mathscr{R}_{lJ}(E)]}, \qquad (10)$$

where the complex R function can be approximated [13] by

$$\mathscr{R}_{lJ}(E)=\tilde{R}_{lJ}(E)+i\pi\tilde{s}_{lJ}(E). \qquad (11)$$

The justification for the approximation and the details of the comparison of the averaged empirical functions with predicted scattering functions, $S^{\rm OMP}_{lJ}(E)$, are treated in more detail in Ref. [11].

Our procedure was to use a Woods-Saxon well with real, surface imaginary, and spin-orbit terms as

TABLE IV. Parametrization for the external R functions. [See Eqs. (6) and (11) for relationship of parameters to the R function.]

J^π	α	β (1/MeV)	$\tilde{s}_{lJ}(\times 10^{+2})$	$\tilde{R}(\bar{E})$
$s_{1/2}$	0.13	0.024	0.39(7) [a]	0.13(1)
$p_{1/2}$	−0.33	0.58	$7.8(10)^{13}_{4.4}$	−0.24(10)
$p_{3/2}$	−0.27	0.30	$5.7(7)^{7.5}_{3.3}$	−0.22(10)

[a]In our notation, 0.39(7) corresponds to 0.39±0.07, etc. α and β uncertainties are discussed in the text. Upper and lower limits are established as in Table III.

TABLE V. Radius and diffuseness parameters for OMP.

	V_r	W_D	$U_{\text{s.o.}}$
r_0 (fm)	1.23	1.25	1.12
a (fm)	0.66	0.54	0.50

$$V(r) = -V_r f(r) - iW_D g(r) - U_{\text{s.o.}} h(r) \vec{l} \cdot \vec{\sigma},$$

where

$$f(r) = \{1 + \exp(r - r_0 A^{1/3})/a\}^{-1},$$

$$g(r) = 4a' \frac{d}{dr} |\{1 + \exp(r - r_0' A^{1/3})/a'\}^{-1}|,$$

$$h(r) = \left[\frac{\hbar}{m_\pi c}\right]^2 \frac{1}{r} \left| \frac{d}{dr} f(r) \right|.$$

The parameters V_r, W_D, and $U_{\text{s.o.}}$ are the well depths for the real, imaginary, and spin-orbit potentials, respectively. The r_0 and a values represent radius and diffuseness parameters for the corresponding portions of the potential.

We performed a least squares adjustment of the real and imaginary depths until the integrated strengths and R_{lJ}^{ext} predicted by the model agreed with our experimental values. The geometry of the model used was taken from work on ^{116}Sn and ^{120}Sn by Guss *et al.* [6] and held constant at the values shown in Table V. The well depth for the spin-orbit potential was likewise held constant in the fitting process.

The predicted results for the s wave R^{ext}, shown by the solid curve in Fig. 5, are indistinguishable from the empirical values. In the case of p waves the predicted results are systematically high throughout most of the region, but are within the error bars. (The dashed curve is to be compared with the ⊙ values and the solid curve with the Δ values.) The latter have error bars of the same magnitude as those for the $p_{1/2}$. The agreement is good and the energy trends of the model predictions closely parallel the experimental trends. The corresponding comparison for the $s_{1/2}$ integrated strength is presented in Fig. 6. The model representation in this case is good up to an energy of 240 keV.

Changes in the real potential, while predominantly affecting the R^{ext}, do influence the integrated strength to a limited extent but the surface imaginary potential depth has the greater influence over this quantity. Despite this interdependence, both average quantities are well described with the same potential parameters.

The experimental results for the component p-wave integrated strengths have been presented earlier in the discussion of strength functions. The solid lines in Fig. 3 represent model predictions based upon parameters deduced from the least squares adjustment, applied separately for the two components. These are seen to describe the data well over the entire energy range. And, this description was achieved with virtually identical model parameters. However, the fits obtained for the average parameters for the two orbital angular momentum states required different depths for both the real and surface imaginary potentials.

The average of the real well depths for s and p waves is consistent with the parametrization found for similar isotopes of tin in the study of Guss *et al.* [6], after suitable adjustments for isotope and energy differences. These results are presented in Table VI with the values from the model deduced by Guss *et al.* It should be noted that their model overestimated the p-wave strength functions by more than 40%. When we used the geometry *and* well depths of Guss *et al.* our model R^{ext} was too high for s waves and too low for the p waves, both by factors of approximately two. An identical comparison held for the model s- and p-wave strengths.

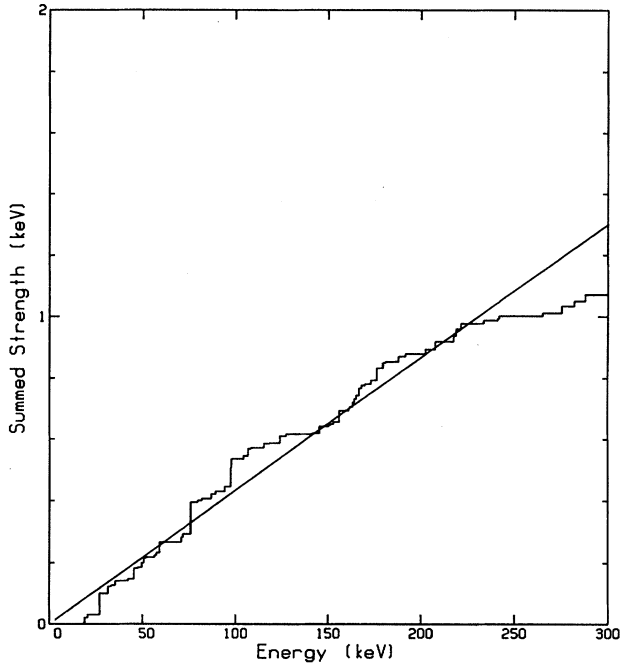

FIG. 6. Experimental integrated strength and model predictions, based upon geometric and potential parameters in Tables V and VI.

Most investigations aimed at elucidating the form of the optical model potential do not include low-energy information in the analysis. It should not be expected that these results would call for an l dependence to the real well depth. In the present study all the data is low energy and one parameter, the s-wave smoothed R function, is most precisely determined at energies approaching zero. We have in addition, information on the energy dependence of this parameter for both l waves (see Fig. 5). Here, as in other similar studies [9], we thus conclude that the real well depth must be deeper for p waves than for s waves to describe the low-energy neutron interaction.

TABLE VI. Spherical optical model parameters. Well depths are in MeV.

	Present work			Guss *et al.*	
	V_r	W_D	$U_{\text{s.o.}}$	V_r	W_D
$s_{1/2}$	46.0	1.0	6.5	48.2	1.0
$p_{1/2}$	50.0	6.2	6.5	48.2	1.0
$p_{3/2}$	50.0	6.6	6.5	48.2	1.0

TABLE VII. Optical model parameters for various geometries. α_V and α_D give the energy dependence of the corresponding well depths.

	Guss [a]			Harper [b]			Rapaport [c]		
	$s_{1/2}$	$p_{1/2}$	$p_{3/2}$	$s_{1/2}$	$p_{1/2}$	$p_{3/2}$	$s_{1/2}$	$p_{1/2}$	$p_{3/2}$
V_r (MeV)	46.0	49.8	49.4	45.2	48.2	48.2	46.4	49.0	51.4
W_D (MeV)	1.0	5.0	5.0	1.9	6.3	6.9	0.9	11.0	6.2
$U_{s.o.}$ (MeV)	6.5	6.5	6.5	5.5	5.5	5.5	6.2	6.2	6.2
α_V (MeV^{-1})		0.30			0.27			0.36	
α_D (MeV^{-1})		0.0			0.053			0.52	

[a] $r_V=1.23$; $r_D=1.25$; $r_{s.o.}=1.12$; $a_V=0.66$; $a_D=0.54$; $a_{s.o.}=0.50$, all in fm.
[b] $r_V=1.26$; $r_D=1.26$; $r_{s.o.}=1.12$; $a_V=0.58$; $a_D=0.40$; $a_{s.o.}=0.50$, all in fm.
[c] $r_V=1.20$; $r_D=1.32$; $r_{s.o.}=1.01$; $a_V=0.70$; $a_D=0.62$; $a_{s.o.}=0.76$, all in fm.

VII. DISCUSSION

Because of the large number of stable isotopes of tin, this element has been studied extensively to gain information on the neutron excess and energy dependences of the parameters of the optical model potential (OMP). Differential elastic scattering and total cross sections for many of the isotopes of tin have been measured by Guss *et al.* [6], Rapaport *et al.* [14], and Harper *et al.* [15] and used to deduce these dependences for the well depths of the potential. In another study which more closely approximates the present work, in type and energy range (0.3–5.0 MeV), Harper *et al.* [16] deduced parameters which represent their total cross section measurements rather well in all but the 2–5 MeV energy region. While there are small nuances of difference in analysis approach and the parameters obtained in the various studies, all have focused on a larger energy range and thus a more complete data set than the present study. Conventional differential elastic scattering and total cross section measurements provide strong constraints on the optical model potential, but generally have little l specificity. Because of the extent of the data in most studies of this type, the geometric parameters are well determined. Since their analyses consider data that is non-partial-wave specific, it is expected that there may be parts of our average quantities which will not be reproduced by the complete parameter set from such studies.

In order to assure that the different geometries of the other studies could not account for the l dependence we observed, we also searched for well depths corresponding to several of these geometries which would best represent all our data. The l dependence persisted in each case, with only the magnitudes of the well depths changing with geometry. Thus it is seen in Table VII that in every case the difference between required s- and p-wave well depths is approximately 2–4 MeV for the real potential and the imaginary potentials differ by more than 4 MeV. It should be noted that not all features of all data sets of the other studies have been properly described by their deduced parameters. The cross sections are low in some cases and high for others. This could be a manifestation of the need for an l dependence, which our data clearly dictate.

Some studies have included l-specific properties as parameters in the model, such as potential scattering radii or strength functions, but none have obtained information on these quantities through direct identification or observation of individual contributions to partial wave samples. For example, Timokhov *et al.* [17] have modeled neutron capture cross sections and transmissions, for all the stable tin isotopes over the energy range 20–1400 keV, in the framework of the Hauser-Feshbach-Moldauer formalism. They have deduced strength functions and potential scattering radii for s- and p-wave interactions. In the present study we have obtained potential scattering radii, in addition to the average scattering functions for each J^π, according to the relation [18]

$$R' = a_c[1-(2l+1)\tilde{R}(E=0)].$$

Comparisons of results from these considerations are presented in Table VIII. They also deduced an OMP and found that not all data can be represented with a single potential. They did not, however, report an l dependence. An increasing body of evidence is accumulating that one must impose an l dependence to an optical model description of results of the analysis of high resolution low energy elastic neutron scattering cross sections [9].

VIII. CONCLUSIONS

The tin isotopes have been the focus of the prediction that possible doorway structure may exist in this mass region, based on evidence presented many years ago for the presence of enhanced $M1$ strength in these isotopes. Though one might expect similar structure for s waves, our analysis of high-resolution neutron total cross section data for ^{122}Sn would suggest little support for this expectation, as seen from the cumulative plots of s wave reduced neutron widths presented in Fig. 6. In earlier calculations, in which doorway structure was postulated in order to account for the low s-wave strength, Shakin [5] predicted the doorways to lie at much higher energies than covered in the present analysis. We are thus able to conclude from this study that any possible doorway structure in these isotopes of tin must lie above 310 keV.

TABLE VIII. Potential scattering radii (fm).

J^π	Present	Timokhov *et al.*	Popov
$1/2^+$	6.3(2) [a]	6.1(2)	6.0(2)
$1/2^-$	8.9(2)		
$3/2^-$	8.8(2)		
p		8.6(3)	9.3(2)

[a] In our notation 6.3(2) corresponds to 6.3 ± 0.2, etc.

Several studies have suggested the need for an l dependence for the real well depth of the OMP, when analyzing the low energy total cross section data. We find further evidence in this isotope of tin. Mahaux and Ngo have recently suggested [19] an alternate interpretation for this result in which a surface potential is included, thereby obviating the need for an l dependence, an interpretation which finds more theoretical support than the former. This elimination of the l dependence is possible because the s- and p-wave functions are approximately 90° out of phase at the nuclear surface. Since the matrix element involves a product of the wave function and the derivative of the potential, the addition of a surface potential to each partial wave will affect only the partial wave whose antinode occurs at the nuclear surface [20]. Application of these ideas to this and other spin-zero isotopes of tin would provide clarification concerning this feature of low energy partial wave analysis of neutron total cross section data.

ACKNOWLEDGMENTS

This work was partially supported by the U.S. Department of Energy under Contract No. DE-FG05-86ER40293 with Middle Tennessee State University. The Oak Ridge National Laboratory is operated by Martin Marietta Energy Systems, Inc. for the Department of Energy under Contract No. DE-AC05-84OR21400.

[1] L. S. Kisslinger and R. A. Sorensen, Rev. Mod. Phys. **35**, 853 (1963).
[2] E. Baranger, in *Advances in Nuclear Physics*, edited by M. Baranger and E. Vogt (Plenum, New York, 1971), p. 261.
[3] T. Fuketa and J. A. Harvey, Oak Ridge National Laboratory Report No. ORNL-3425, 1962 (unpublished), p. 36.
[4] J. A. Harvey and T. Fuketa, in *Proceedings of the Conference on Study of Nuclear Structure with Neutrons*, edited by M. Neve de Mervergnies, P. Van Assche, and J. Vervier (North-Holland, Amsterdam, 1966), p. 527.
[5] C. Shakin, Ann. Phys. **22**, 373 (1963).
[6] P. P. Guss, R. C. Byrd, C. R. Howell, R. S. Pedroni, G. Tungate, and R. L. Walter, Phys. Rev. C **39**, 405 (1989).
[7] D. C. Larson, N. M. Larson, J. A. Harvey, N. W. Hill, and C. H. Johnson, Oak Ridge National Laboratory Report No. ORNL/TM-8203, Oak Ridge, Tennessee, 1984 (unpublished).
[8] D. C. Larson, N. M. Larson, and J. A. Harvey, Oak Ridge National Laboratory Report No. ORNL/TM-8880, Oak Ridge, Tennessee, 1984 (unpublished).
[9] C. H. Johnson, in *Neutron-Nucleus Collisions: A Probe of Nuclear Structure*, edited by J. Rapaport, R. W. Finlay, S. M. Grimes, and F. S. Dietrich, AIP Conf. Proc. No. 124 (AIP, New York, 1985), p. 446.
[10] N. M. Larson, Oak Ridge National Laboratory Report No. ORNL/TM-9179/R2, Oak Ridge, Tennessee, 1989 (unpublished).
[11] C. H. Johnson, R. F. Carlton, and R. R. Winters, Phys. Rev. C **39**, 415 (1989).
[12] F. J. Dyson and M. L. Mehta, J. Math. Phys. **4**, 489 (1963).
[13] C. H. Johnson, C. Mahaux, and R. R. Winters, Phys. Rev. C **32**, 359 (1985).
[14] J. Rapaport, M. Mirzaa, H. Hadizadeh, D. E. Bainum, and R. W. Finlay, Nucl. Phys. **A341**, 56 (1980).
[15] R. W. Harper, J. L. Weil, and J. D. Brandenberger, Phys. Rev. C **30**, 1454 (1984).
[16] R. W. Harper, T. W. Godfrey, and J. L. Weil, Phys. Rev. C **26**, 1432 (1982).
[17] V. M. Timokhov, M. W. Bokhovko, A. G. Isakov, L. E. Kazakov, V. N. Kononov, G. N. Manturov, E. D. Poletaev, and V. G. Pronyaev, Sov. J. Nucl. Phys. **50**, 375 (1989).
[18] A. B. Popov and G. S. Samosvat, Radiat. Eff. (G.B.) **93**, 285 (1986).
[19] C. Mahaux and H. Ngo, Nucl. Phys. **A431**, 486 (1984).
[20] C. H. Johnson and R. R. Winters, Phys. Rev. C **37**, 2340 (1988).